Nanoscale

PAPER

View Article Online
View Journal | View Issue

Cite this: *Nanoscale*, 2023, **15**, 5044

Atomic layer deposition of SnO_2 using hydrogen peroxide improves the efficiency and stability of perovskite solar cells†

Sang-Uk Lee,[a] Hyoungmin Park,[b] Hyunjung Shin [b,c] and Nam-Gyu Park [*a,c]

Low-temperature processed SnO_2 is a promising electron transporting layer in perovskite solar cells (PSCs) due to its optoelectronic advantage. Atomic layer deposition (ALD) is suitable for forming a conformal SnO_2 layer on a high-haze substrate. However, oxygen vacancy formed by the conventional ALD process using H_2O might have a detrimental effect on the efficiency and stability of PSCs. Here, we report on the photovoltaic performance and stability of PSCs based on the ALD-SnO_2 layer with low oxygen vacancies fabricated *via* H_2O_2. Compared to the ALD-SnO_2 layer formed using H_2O vapors, the ALD-SnO_2 layer prepared *via* H_2O_2 shows better electron extraction due to a reduced oxygen vacancy associated with the highly oxidizing nature of H_2O_2. As a result, the power conversion efficiency (PCE) is enhanced from 21.42% for H_2O to 22.34% for H_2O_2 mainly due to an enhanced open-circuit voltage. Operational stability is simultaneously improved, where 89.3% of the initial PCE is maintained after 1000 h under an ambient condition for the H_2O_2-derived ALD SnO_2 as compared to the control device maintaining 72.5% of the initial PCE.

Received 9th December 2022,
Accepted 3rd February 2023

DOI: 10.1039/d2nr06884b

rsc.li/nanoscale

Introduction

Since the report on all-solid-state PSCs with a PCE of 9.7% and nondegraded stability for 500 h in 2012,[1] PSCs have received tremendous attention due to low cost and high efficiency. As a result, a certified PCE of 25.7% has been achieved in 2022.[2] Such superb photovoltaic performance was realized by excellent intrinsic optoelectronic properties of the perovskite material with high absorption coefficient, diffusion length, defect-tolerance properties,[3–6] and compositional engineering and manufacturing processes such as interfacial, additive, and precursor engineering.[7–11] Besides the perovskite layer, charge transport materials and junction between perovskite and charge transport layers are critical in determining photovoltaic performance. Thus, the selection of suitable materials and methods to fabricate charge transport layers are important to achieving high efficiency and stability of PSCs. For the n-i-p device structure, the electron transport layer (ETL) plays a crucial role, not only in electron extraction but also in providing a substrate for perovskite film growth. Among the studied ETLs, the wide bandgap SnO_2 formed at low temperatures is widely used for ETL because of high carrier mobility, low-temperature processibility, and photo-inactive nature under UV illumination.[12–15] Various coating methods have been reported to fabricate SnO_2 thin films including chemical bath deposition,[16] spray-pyrolysis,[17] and atomic layer deposition (ALD).[18–21] ALD is one of the beneficial techniques for conformal and uniform coating compared to other methods.[22–24] When using H_2O and the tetrakis(dimethylamino) tin (TDMASn) precursor to deposit SnO_2 thin films in ALD, compared with hydrogen peroxide (H_2O_2) and ozone (O_3), an oxygen vacancy is often generated due to slow kinetics associated with uneasy removal of ligands in the precursor from the SnO_2 surface.[25,26] As a result, these oxygen vacancies can cause poor performance and instability because they act as a recombination site for carriers.[27,28] Thus, it is interesting to compare the photovoltaic performance of PSCs between the H_2O-derived ALD SnO_2 and the H_2O_2-derived one.

Here, we report on the highly oxidizing H_2O_2 as an oxygen vapor source for preparing the SnO_2 thin film in ALD. Photovoltaic performance and stability for the H_2O_2-derived SnO_2 films are compared with those for the H_2O-derived ones. Better extraction of the photoexcited electrons from perovskite to SnO_2 is observed for the H_2O_2-derived SnO_2 than for the

[a]*School of Chemical Engineering, Center for Antibonding Regulated Crystals, Sungkyunkwan University, Suwon 16419, Republic of Korea.*
E-mail: npark@skku.edu
[b]*Department of Energy Science, Sungkyunkwan University, Suwon 16419, Republic of Korea*
[c]*SKKU Institute of Energy Science and Technology (SIEST), Sungkyunkwan University, Suwon 16419, Republic of Korea*

† Electronic supplementary information (ESI) available. See DOI: https://doi.org/10.1039/d2nr06884b

H_2O-derived one due to reduced surface oxygen defects. As a result, higher photovoltaic performance and improved stability are achieved using H_2O_2 during ALD. This work provides important insight into the carrier material design for oxide films in ALD.

Results and discussion

The ALD process is schematically illustrated in Fig. 1, where one cycle of ALD comprising two half cycles in between purging cycles is repeated to form oxide thin films. In the first half cycle shown in Fig. 1(a), the gaseous TDMASn precursor is pulsed to react with the hydroxyl-functionalized surface on the substrate, followed by purging Ar to remove the byproduct of dimethylamine and unreacted precursor. For the second half cycle in Fig. 1(b), an oxygen source, such as H_2O or H_2O_2 is pulsed to react with the surface adsorbed DMA-Sn-O, followed by purging Ar to eliminate byproducts of dimethylamine and O_2. Since oxygen defect may be formed due to the surface hydroxyl group, leading to $SnO_{2-x}(OH)_x$, an oxygen source with higher oxidizing and better proton transfer capability, such as H_2O_2, is expected to be better in defect-less SnO_2.[29–31]

X-ray photoelectron spectroscopy (XPS) was carried out to investigate the oxidation state of tin and oxygen vacancy of the ALD-deposited SnO_2 film. As shown in Fig. 2(a), the binding energies of Sn $3d_{5/2}$ (487.18 eV) and Sn $3d_{3/2}$ (495.58 eV) for the H_2O_2-derived SnO_2 are slightly higher than the corresponding 486.88 eV and 495.33 eV for the H_2O-derived one. The spin–orbit splitting of about 8.4 eV and binding energies indicate that the oxidation state of tin is close to being tetravalent.[32] The slightly higher binding energies observed for the H_2O_2-derived SnO_2 implies that the oxidation state of tin in the H_2O_2-derived SnO_2 is relatively higher than that in the H_2O-derived one,[33–36] which might be due to the stronger oxidizing characteristics of H_2O_2. Oxygen 1s XPS spectra in Fig. 2(b) for H_2O and Fig. 2(c) for H_2O_2 are deconvoluted into two peaks that correspond to the oxygen on the surface of SnO_2 (O_{Sn}) and chemisorbed oxygen or hydroxyl-related oxygen (O_{OH}).[37–40] The binding energies for each species and fraction of O_{OH} are listed in Table S1.† The fraction of O_{OH} decreased from 25.47% to 21.36% upon replacing H_2O with H_2O_2, indicative of the suppression of oxygen vacancy (defect) by H_2O_2 during the preparation of SnO_2.

To understand the dependence of perovskite morphology on the SnO_2 film formed from different oxygen sources in the ALD process, scanning electron microscopy (SEM) images of the perovskite films were collected. According to the cross-sectional SEM images shown in Fig. 3(a) and (c), the mean thickness of the perovskite film was slightly thicker for the H_2O_2-derived SnO_2 (549.4 ± 69.2 nm) than the H_2O-derived one (518.8 ± 29.3 nm) and the entire film morphology including the surface flatness is better for the perovskite film grown on the H_2O_2-derived SnO_2. This indicates that the H_2O_2-derived SnO_2 layer is beneficial for the growth of high-quality perovskite film. Furthermore, the perovskite grain size was also increased from 893.0 nm for H_2O to 1046.9 nm for H_2O_2 (Fig. 3(b) and (d)), which is beneficial for the reduction of

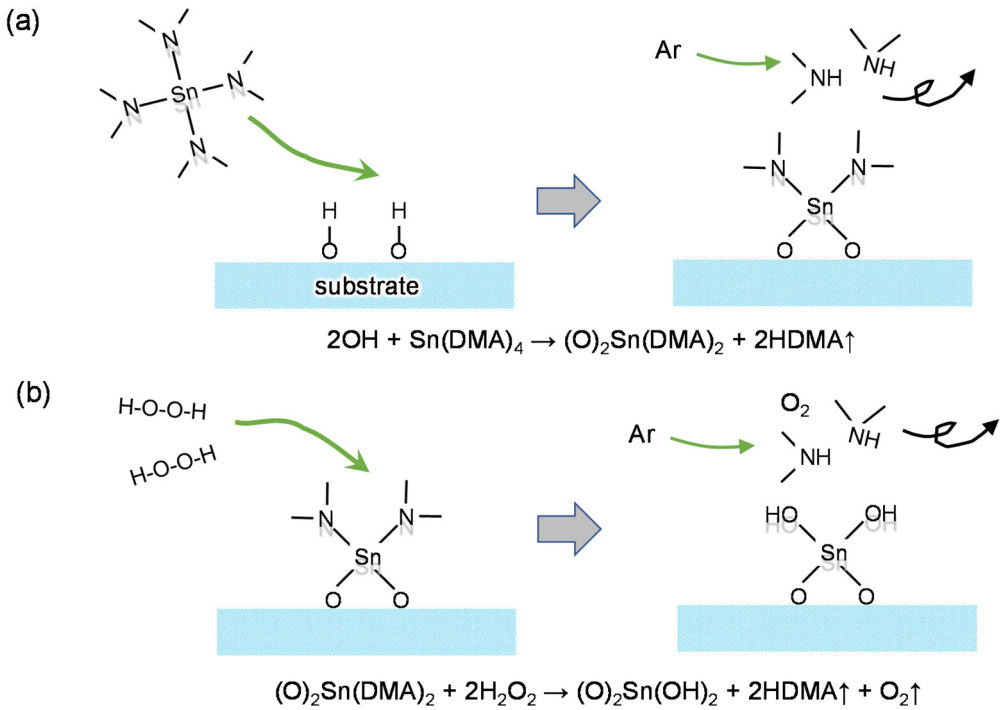

Fig. 1 The schematic illustration of (a) the first half cycle and (b) the second half cycle of the ALD process to form SnO_2 using TDMASn and H_2O_2, together with chemical reactions. A hydroxyl-functionalized substrate was assumed.

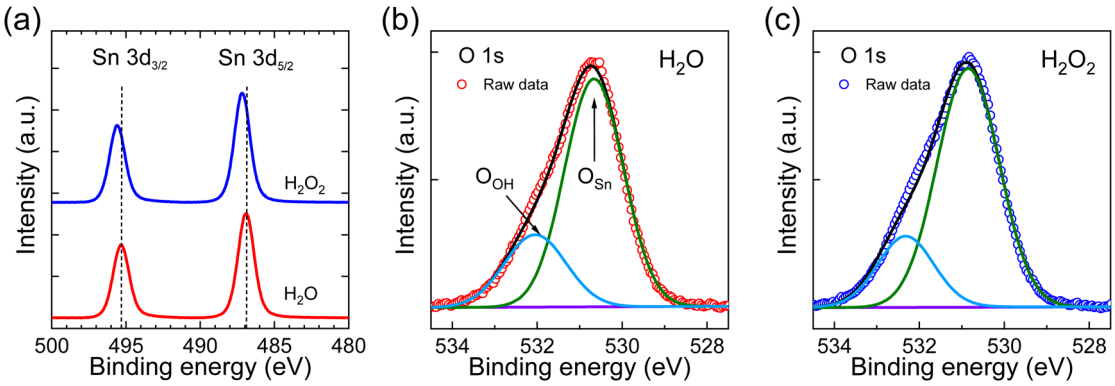

Fig. 2 (a) Sn 3d and (b and c) O 1s XPS spectra of the ALD-SnO_2 films based on H_2O and H_2O_2 oxygen source. The binding energy was calibrated using the C 1s binding energy of 284.78 eV. The raw data (black empty circles) in O 1s data were deconvoluted to two peaks (blue lines: hydroxyl oxygen (O_{OH}), green lines: oxygen in Sn–O (O_{Sn}), and purple lines: baseline).

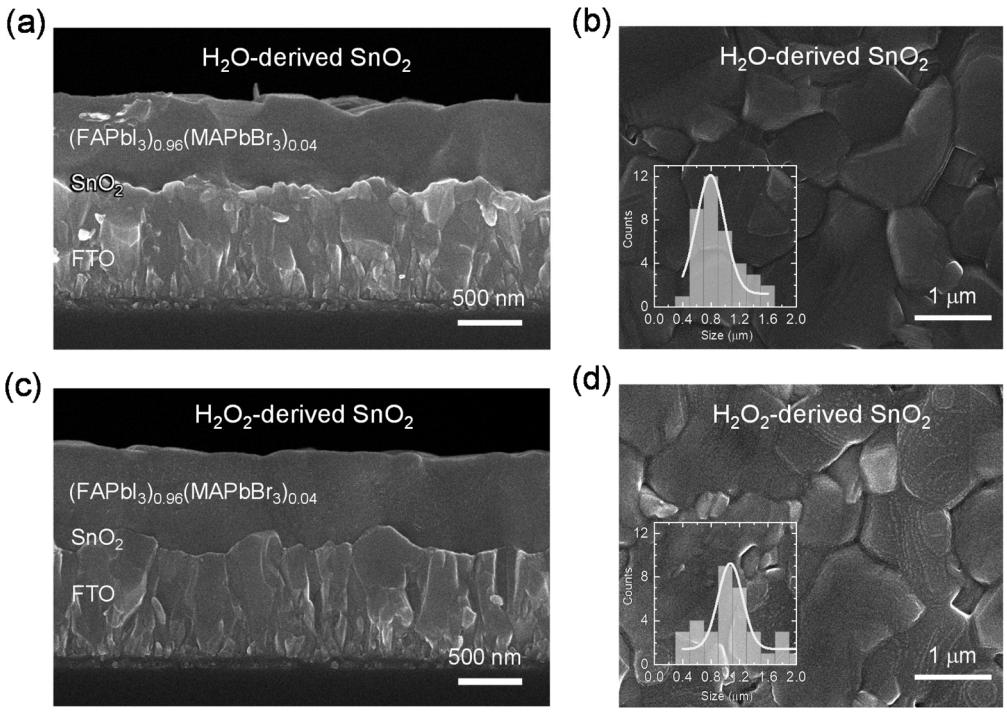

Fig. 3 (a and c) Cross-sectional and (b and d) top-view SEM images of the perovskite films formed on (a and b) the H_2O-derived SnO_2 and (c and d) the H_2O_2-derived SnO_2. Insets are size distributions.

grain boundaries. A contour-line-like surface morphology observed from the H_2O_2-derived SnO_2 is indicative of improvement of the perovskite crystallinity.[41]

To understand the change in the surface morphology of ALD-SnO_2 depending on H_2O and H_2O_2, top-view SEM and atomic force microscopy (AFM) images were captured, as shown in Fig. S1.† Although the difference in surface morphology of the ALD-SnO_2 is hard to figure out from the top-view SEM images, the surface roughness in the AFM image was reduced from 36.43 nm for H_2O to 32.02 nm for H_2O_2. The reduced surface roughness of the SnO_2 film would be beneficial for better contact with the perovskite,[42] which is one of the factors responsible for the improved V_{oc} and FF. To investigate the effect of the oxygen source on the optical properties of the perovskite film and the photon-to-electron conversion efficiency of PSCs in the ALD process, UV-Vis spectroscopy and external quantum efficiency (EQE) were performed and the data are shown in Fig. S2.† The absorbance of the perovskite films hardly changed regardless of the oxygen source. In addition, an optical band gap calculated from the Tauc plot was about 1.55 eV, which is also unaffected by the oxygen source. The EQE spectral shape for H_2O_2 is almost identical to that for H_2O, except for the slightly higher integrated J_{sc} of 23.87 mA cm^{-2} for H_2O_2 than 23.61 mA cm^{-2} for H_2O.

The effect of the oxygen source on charge separation and carrier lifetime was studied using steady-state photoluminescence (SSPL) and time-resolved photoluminescence (TRPL). As seen in Fig. 4(a), the PL emission intensity of the bare perovskite film was significantly decreased in the presence of the SnO_2 layer due to electron injection from perovskite to SnO_2. PL quenching is more pronounced for the H_2O_2-derived SnO_2 than for the H_2O-derived one, which is probably due to the reduced oxygen defects, as observed in the O 1s XPS study (see Fig. 2). The TRPL decay curves in Fig. 4(b) were fitted with a biexponential decay equation of $I(t) = I_0 + A_1\exp(-(t - t_0)/\tau_1) + A_2\exp(-(t - t_0)/\tau_2)$, where $I(t)$ is the time-dependent PL intensity, τ_1 is the fast decay component attributed to the quenching of charge carriers in the interface, and τ_2 is the slow decay component related to the radiative recombination of free charge carriers in the bulk.[43–45] The detailed parameters are summarized in Table S2.† The perovskite film deposited on the glass substrate showed the longest lifetime of τ_1 = 104.5 ns and τ_2 = 1957.3 ns because there is no layer to transfer the charges from the perovskite layer, which is consistent with the values reported elsewhere.[46] For the perovskite film deposited on the H_2O_2-derived SnO_2, τ_1 and τ_2 were reduced to 46.7 ns and 390.3 ns, respectively, while 71.3 ns and 486.7 ns were observed for the H_2O-derived one. The reduced time constants ascribed to the charge transfer from perovskite to SnO_2 and the faster decay in PL for the H_2O_2-derived SnO_2 are indicative of the faster charge separation, probably due to the improved interface.[47]

Dark current–voltage (I–V) characteristics of the electron-only device (FTO/ETL/Au) were investigated to analyze the conductivity of the ALD-SnO_2 (Fig. 4(c)). Conductivity can be estimated from $\sigma = Id/VA$, where σ, d, and A are the conductivity, the thickness of the ETL film, and the area of the sample, respectively.[48,49] Although SnO_2 is a wide-bandgap oxide that is essentially an insulator, the electrical conductivity of the H_2O_2-derived SnO_2 film was estimated to be 4.43×10^{-4} mS cm^{-1}, which is slightly higher than 3.11×10^{-4} mS cm^{-1} of the H_2O-derived SnO_2. The improvement of charge extraction transport at the H_2O_2-derived SnO_2 is thus related to the relatively improved conductivity due to surface passivation, which seems to contribute to the improvement of FF.[48,50] To examine the charge recombination and electron transport ability of ETL in the full device structure (FTO/SnO_2/perovskite/spiro-MeOTAD/Au), transient photovoltage (TPV) and transient photocurrent (TPC) decay were measured (Fig. 4(d) and (e)) and fitted by using a biexponential decay equation.[51,52] TPV decay was measured at open-circuit conditions, where the increase of photovoltage lifetime is indicative of the longer recombination lifetime of holes and electrons. The TPV decay time for the H_2O_2-derived SnO_2 was estimated to be 0.530 ms,

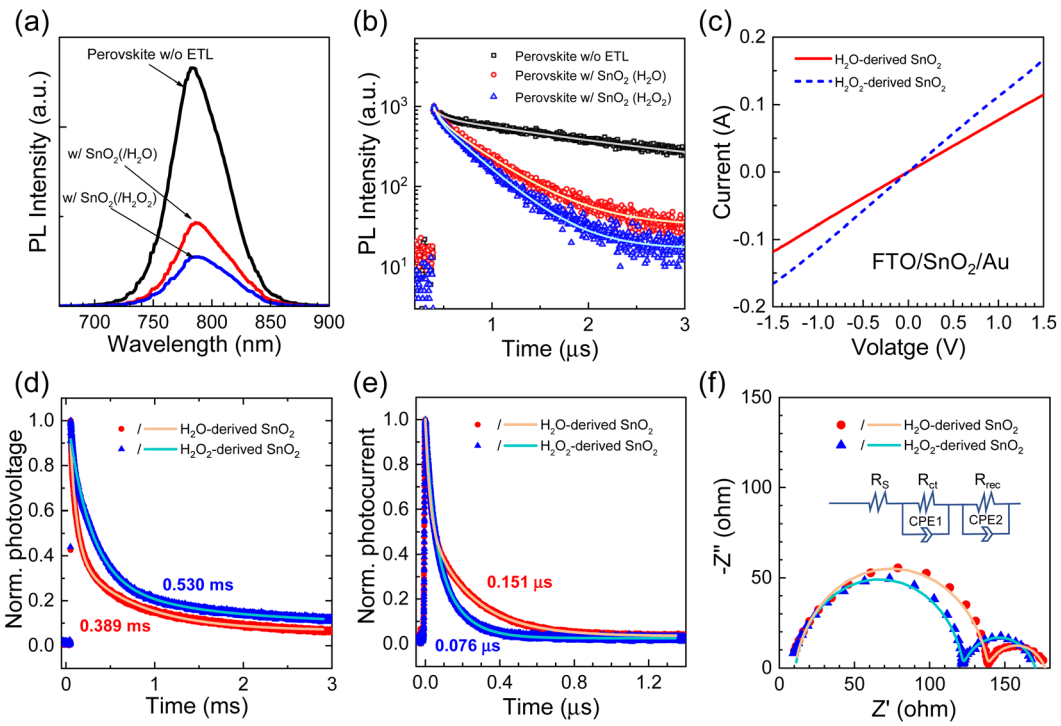

Fig. 4 (a) Steady-state PL and (b) TRPL of perovskite films deposited on glass with and without ALD-SnO_2 layer. Lines represent the fitted results in TRPL. (c) Dark I–V characteristics of the FTO/SnO_2/Au devices. (d) TPV and (e) TPC data. Data were fit with the biexponential decay equation, which is represented as lines. (f) Nyquist plots obtained in the frequency range of 1 MHz to 0.1 Hz under one sun illumination at a bias of 1.0 V with the device structure of the FTO/SnO_2/perovskite/Spiro-MeOTAD/Au. Inset is the equivalent circuit, where R_s, R_{ct}, R_{rec}, CPE1, and CPE2 represent series resistance, resistance for charge transport, resistance for charge recombination, constant phase element 1, and constant phase element 2, respectively.

which is longer than 0.389 ms for the H_2O-derived SnO_2, suggesting that the SnO_2 layer formed by H_2O_2 vapor is more beneficial for the reduction of the nonradiative recombination.[53,54] TPC decay measured under short-circuit condition, where the decrease in photocurrent decay time implies that charge carrier transport becomes faster. The photocurrent decay was shortened from 0.151 μs for the H_2O case to 0.076 μs upon using H_2O_2. According to the data from TPV and TPC, higher V_{oc} for the H_2O_2-derived SnO_2 is attributed to the reduction of recombination.

To further analyze the increase of V_{oc} and FF for the H_2O_2-derived SnO_2, electrochemical impedance spectroscopy (EIS) study was carried out to examine the interfacial charge transfer and recombination. In Fig. 4(f), Nyquist plots of the full devices (FTO/SnO_2/perovskite/Spiro-MeOTAD/Au) are shown in the frequency range of 1 MHz to 0.1 Hz under one sun illumination at a bias of 1.0 V. Two semicircles were observed, where the first semicircle in the high-frequency region is related to the charge transport resistance (R_{ct}) at the interface and the second semicircle in the low-frequency region correlates with the charge recombination resistance (R_{rec}).[55–57] R_{ct} for the H_2O_2-derived SnO_2 is 111.2 Ω, which is lower than 127.9 Ω for the H_2O-derived one. On the other hand, R_{rec} was increased from 38.3 Ω for the H_2O-derived SnO_2 to 48.4 Ω for the H_2O_2-derived SnO_2. The values obtained for R_{ct} and R_{rec} under one sun illumination at a bias of 1.0 V close to the V_{oc} are consistent with those reported elsewhere.[55,56] In addition, the fact that R_{rec} is lower than R_{ct} might be due to the dielectric relaxation by an interfacial ion reorganization and charge accumulation of perovskite in the low-frequency region under one sun illumination.[56–58] Thus, the lower R_{ct} and higher R_{rec} for the H_2O_2-derived SnO_2 than for the H_2O-derived one is responsible for higher FF and V_{oc} due to the improved charge transport and reduced recombination.[37,59]

The energy band alignment of ETL and the perovskite layer were studied using ultraviolet photoelectron spectroscopy

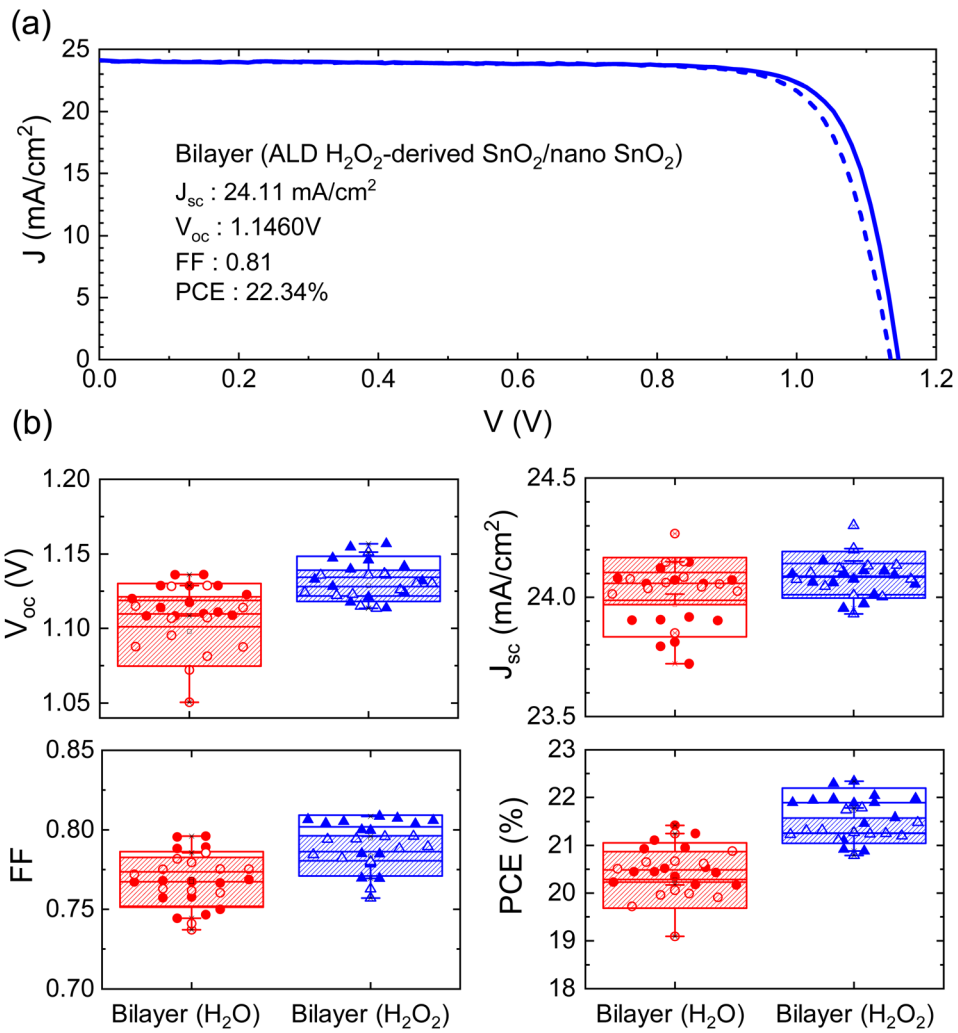

Fig. 5 (a) *J*–*V* curves of the best performing PSC with a bilayer of ALD-SnO_2/spin-coated SnO_2. Dashed and solid lines represent forward and reverse scanned data, respectively. (b) Statistical photovoltaic parameters of J_{sc}, V_{oc}, FF, and PCE for a bilayer SnO_2 with the H_2O-derived SnO_2 and the H_2O_2-derived one. Diagonal lines and empty squares represent forward-scanned and reverse-scanned data, respectively.

(UPS), Fig. S3,† and UV-Vis spectroscopy, Fig. S4.† The work function was measured by the difference between He I radiation (21.22 eV) and $E_{cut\text{-}off}$ (cut-off energy in the high binding energy region). The valence band maximum (VBM) can be determined by the sum of the Fermi level acquired with the work function and the energy obtained in the low binding energy region of the logarithmic-scale curve (Fig. S3†). Finally, the conduction band maximum (CBM) can be determined using an optical bandgap estimated by the Tauc plot (Fig. S4 (a)†). The energy band diagram is represented in Fig. S4(b).† The band gap of the SnO_2 layer (3.96 eV) is unchanged; however, the CBM of the H_2O_2-derived SnO_2 is upshifted from −4.65 eV to −4.53 eV as compared to the H_2O-derived one, which is closer to CBM of −4.32 eV for perovskite. The Fermi level is also upshifted from −5.15 eV to −5.03 eV by changing the oxygen source from H_2O to H_2O_2, which is also closer to that of −4.89 eV for perovskite. Thus, the band alignment between perovskite and the H_2O_2-derived SnO_2 is beneficial for better V_{oc} and FF.[60]

The current density–voltage (J–V) curves and photovoltaic parameters for the H_2O- and H_2O_2-derived SnO_2 films are shown in Fig. S5 and Table S3.† The reverse scanned PCE for the H_2O-derived SnO_2 is 17.71% with short-circuit photocurrent density (J_{sc}) of 24.20 mA cm^{-2}, open-circuit voltage (V_{oc}) of 1.0685 V, and fill factor (FF) of 0.69. The device with the H_2O_2-derived SnO_2 improves PCE to 19.09% mainly due to the enhanced V_{oc} of 1.0973 V and FF of 0.72 with a similar J_{sc} of 24.30 mA cm^{-2}. The improvement of V_{oc} and FF might be attributed to the improved interface between the H_2O_2-derived SnO_2 and perovskite.

Since the PCE was not as high as the reported value of over 20%, the ALD-SnO_2 layer was over-deposited with colloidal SnO_2 *via* the spin-coating process. Fig. 5(a) shows the J–V curves of the best-performing PSCs based on the bilayered SnO_2 comparing the H_2O- or H_2O_2-derived ALD SnO_2 film that was overcoated with the colloidal SnO_2 *via* spin-coating. The photovoltaic parameters are listed in Table S4.† The bilayer SnO_2 films exhibit higher PCEs than the only ALD-SnO_2 case. The reverse scanned PCE of 21.42% was achieved from the bilayer SnO_2 based on the H_2O-derived SnO_2 due to J_{sc} of 24.07 mA cm^{-2}, V_{oc} of 1.1175 V, and FF of 0.80, whereas higher PCE of 22.34% was obtained from the bilayer based on the H_2O_2-derived SnO_2 mainly due to the increased V_{oc} of 1.1460 V. The statistical photovoltaic parameters shown in Fig. 5(b–e) and Table S5† indicate that the average PCE of 21.73 ± 0.44% for the H_2O_2 approach is higher than the 20.64 ± 0.38% observed for the H_2O method.

Steady-state PCE was examined for 1200 s at the maximum power point under one sun illumination without encapsulation. Fig. 6(a) shows that PSC based on the H_2O_2-derived ALD-SnO_2/colloidal SnO_2 bilayer maintains 97.90% of the initial PCE, whereas PCE declined down to 95.84% for the H_2O-derived ALD-SnO_2/colloidal SnO_2 bilayer. Finally, storage stability was investigated for 1000 h at ambient conditions of a temperature of 25 ± 5 °C and relative humidity of 30 ± 5%. Fig. 6(b) shows that 89.3% of the initial PCE was maintained

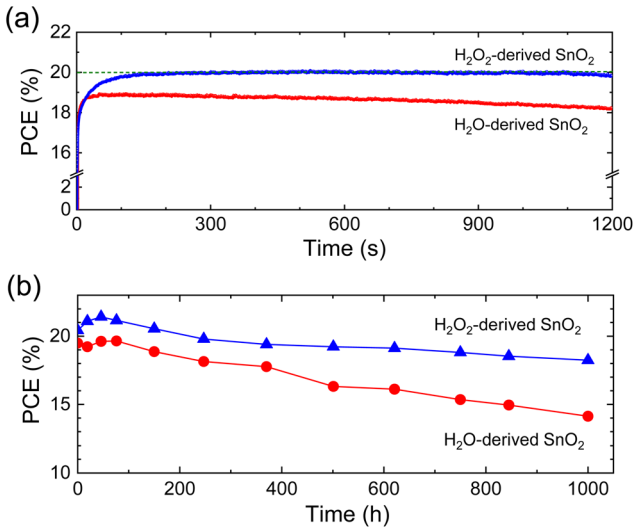

Fig. 6 Comparison of the stability of the H_2O_2-derived SnO_2-based PSC with the H_2O-derived SnO_2-based PSC using (a) steady-state PCE measured at maximum power points (0.922 V for H_2O and 0.935 V for H_2O_2) for 1200 s and (b) storage stability for 1000 hours under a relative humidity of about 30% at room temperature.

for the H_2O_2-derived SnO_2 system after 1000 h, while 72.5% of the initial PCE was retained for PSC based on the H_2O-derived SnO_2. Normalized photovoltaic parameters are presented in Fig. S6,† where the degraded performance in the H_2O-derived SnO_2 system is mainly due to the relatively pronounced degradation of FF. A relatively poor interface between the perovskite and the H_2O-derived SnO_2 might accelerate the degradation of FF. It has been reported that the charges trapped between the ETL and perovskite layer by the interfacial defects could initiate degradation of the performance and stability of PSCs under the moisture condition.[61] Thus, it is important to manage the ETL surface for improving the stability and efficiency of PSCs and our work can give important insight into the control of the SnO_2 surface *via* the oxygen source in ALD.

Conclusions

The photovoltaic performance and stability of PSCs based on ALD-SnO_2 were studied depending on the oxygen source of H_2O and H_2O_2. The surface oxygen defect of ALD-SnO_2 was reduced by changing H_2O with H_2O_2. As a result, the ALD-SnO_2/perovskite interface was improved by using H_2O_2 and thereby, the separation of the excited electrons was better for the H_2O_2-derived SnO_2 than for the H_2O-derived SnO_2. Since the ALD-SnO_2 plays a substrate role, the perovskite film grown at the H_2O_2-derived SnO_2 layer was better in quality than that grown at the H_2O-derived one. PCE of 22.34% was achieved using the H_2O_2-derived ALD-SnO_2, which was better than that obtained using the conventional oxygen source of H_2O in ALD. Furthermore, the improved SnO_2/perovskite interface using H_2O_2 led to the enhancement of device stability.

From the current study, the control of SnO_2 defects is found to be critical in achieving better efficiency and stability of PSCs.

Experimental

Synthesis of materials

Formamidnium iodide, $HC(NH_2)_2I$ (FAI), was synthesized by reacting 30 mL hydroiodic acid (57 wt% in water, Sigma Aldrich) with 20 g of formamidnium acetate (99%, Sigma Aldrich) in an ice bath for 1 h. The brown precipitate was collected by an evaporating solvent at 60 °C for 30 min using a rotary evaporator. The collected powder was washed with diethyl ether (>99.0%, Sigma Aldrich) to obtain a white precipitate. The product was recrystallized in ethyl alcohol (99.9%, Sigma Aldrich). The recrystallization process was repeated three times to achieve pure FAI powder that was finally washed with diethyl ether. The FAI powder was collected by filtration and dried for 24 h under a vacuum. Methylammonium bromide, CH_3NH_3Br (MABr), was synthesized in a similar method by using hydrogen bromide (HBr, 48 wt% in H_2O, Sigma-Aldrich) and methylamine (CH_3NH_2, 40% in methanol, TCI).

The $FAPbI_3$ single crystals were synthesized by inverse temperature crystallization using a 1.6 M γ-butyrolactone (GBL, 99.5%, SamChun Chemicals) solution of equimolar FAI and PbI_2 (99%, Acros) at 80 °C for 30 min and at 130 °C for 3 h. The product was washed with acetonitrile and diethyl ether, followed by drying at 150 °C for 30 min. The $MAPbBr_3$ single crystals were synthesized in a similar method by using $PbBr_2$ (>98%, Sigma Aldrich) and the synthesized MABr in *N*,*N*′-dimethylformamide (DMF, 99.8% anhydrous, Sigma Aldrich).

Device fabrication

Fluorine-doped tin oxide (FTO) conductive glass substrates (2.4 cm × 2.4 cm, Pilkington, TEC-8, 8 Ω sq^{-1}) were ultrasonically cleaned with detergent, deionized (DI) water, acetone, and ethanol in sequence for 10 min. The cleaned FTO substrates were treated with ultraviolet ozone (UVO) for 40 min before the deposition of the SnO_2 layer by ALD. For the deposition of SnO_2 by a hand-made ALD system, H_2O or H_2O_2 (35 wt% in H_2O, Sigma Aldrich) as an oxygen source and tetrakis(dimethylamino) tin(IV) (TDMASn) (EGCHEM Co., Ltd (Daejeon, Korea)) as a tin precursor were used. The TDMASn precursor was maintained at 50 °C and the deposition was carried out at 100 °C with 84 cycles to obtain 10 nm thickness. One cycle was composed of TDMASn pulse for 0.3 s, Ar purging for 12 s, oxygen source pulse for 0.05 s, and Ar purging for 17 s,[21] under 5×10^{-2} torr with Ar flow of 30 sccm were performed. For the improvement of the photovoltaic performance of PSCs, the ALD-SnO_2 layer was further overcoated with colloidal SnO_2 by spin coating a 2 wt% aqueous colloidal SnO_2 solution (15 wt% stock solution (Alfa Aesar) was diluted) at 4000 rpm for 20 s, which was sintered at 190 °C for 30 min on a hot plate.

The $(FAPbI_3)_{0.96}(MAPbBr_3)_{0.04}$ perovskite precursor solution was prepared by mixing 972.3 mg and 30.7 mg of the synthesized $FAPbI_3$ and $MAPbBr_3$ single crystals, respectively, in 111 μL of dimethyl sulfoxide (DMSO, >99.5%, Sigma Aldrich) and 889 μL of DMF, where 32.4 mg MACl was added as an additive. The perovskite solution was spin-coated on the SnO_2 layer at 1000 rpm for 5 s and 5000 rpm for 20 s, where 1 mL of diethyl ether was dripped on the rotating substrate at 10 s before the end of spin coating, followed by annealing at 150 °C for 15 min and 100 °C for 15 min on a hot plate. The 2,2′,7,7′-tetrakis-(*N*,*N*-di-4-methoxyphenylamino)-9,9′-spirobifluorene (spiro-MeOTAD) stock solution was prepared by mixing 90 mg of spiro-MeOTAD (99%, Sigma Aldrich), 39.5 μL of 4-*tert*-butyl pyridine (4-*t*BP, 98%, Sigma Aldrich), 23 μL of lithium bis(trifluoromethanesulfonyl)imide (Li-TFSI) stock solution (520 mg Li-TSFI (Sigma Aldrich) in 1 mL ACN (99.8%, Sigma Aldrich)) and 10 μL of tris(2-(1*H*-pyrazol-1-yl)-4-*tert*-butylpyridine) cobalt (III) tri[bis(trifluoromethane)sulfonimide] (Co-TFSI) stock solution (375 mg Co-TSFI (Sigma Aldrich) in 1 mL ACN) in 1 mL of chlorobenzene (99.8%, Sigma Aldrich). 25 μL of spiro-MeOTAD solution was spin-coated on the perovskite film at 3000 rpm for 30 s. Finally, a ~70 nm-thick Au electrode was deposited by a thermal evaporator.

Characterization

Current density–voltage (*J*–*V*) characteristics were obtained using a Keithely 2400 source meter under AM 1.5G one sun (100 mW cm^{-2}) illumination using a solar simulator (Oriel Sol 3A, class AAA) equipped with 450 W Xenon lamp (Newport 6280NS). The light intensity was adjusted by an NREL-calibrated Si solar cell having a KG-5 filter. The aperture area was 0.125 cm^2. X-ray photoelectron spectroscopy (XPS) was measured using the ESCALAB 250 XPS system (Thermo Fisher Scientific) with Al Kα X-ray radiation (1486.6 eV). Ultraviolet photoelectron spectroscopy (UPS) was performed with the ESCALAB 250 XPS system (Thermo Fisher Scientific) using He I (21.2 eV). External quantum efficiency (EQE) spectra were obtained using a QEX-7 series system (PV measurements Inc.) by a monochromatic beam generated from a 75 W xenon source lamp (USHIO, Japan) in DC mode. Absorption spectra were obtained using a UV-vis spectrometer (Lambda 45, PerkinElmer). PL was measured using a Quantarus Tau compact fluorescence lifetime spectrometer (Quantarus Tau C11367 12, Hamamatsu) with a 464 nm laser pulsed at a repetition frequency of 10 MHz for steady-state PL and 5 MHz for TRPL. Electrochemical impedance spectroscopy data were collected using an Autolab 302B from a frequency range of 10^{-1} to 10^6 Hz and fitted using the Z-view software.

Author contributions

N.-G. P. and S.-U. L. conceived the idea and wrote the manuscript. S-U. L. carried out the fabrication of devices, measurements, and analysis of the data. H. P. and S.-U. L. constructed a homemade ALD. H. S. provided the methodology for ALD deposition and edited the manuscript.

Conflicts of interest

There are no conflicts to declare.

Acknowledgements

This work was supported by the National Research Foundation of Korea (NRF) grants funded by the Ministry of Science and ICT (MSIT) of Korea under contracts NRF-2021R1A3B1076723 (Research Leader Program) and NRF-2022M3J1A1063226 and NRF-2022M3J1A1085280 (Carbon Neutral Technology Program). H. S. also acknowledges financial support with NRF-2019R1A2C3009157. This work was in part supported by the Korea Evaluation Institute of Industrial Technology under contract 20016588.

References

1 H.-S. Kim, C.-R. Lee, J.-H. Im, K.-B. Lee, T. Moehl, A. Marchioro, S.-J. Moon, R. Humphry-Baker, J.-H. Yum, J. E. Moser, M. Grätzel and N.-G. Park, *Sci. Rep.*, 2012, **2**, 591.
2 M. Kim, J. Jeong, H. Lu, T. K. Lee, F. T. Eickemeyer, Y. Liu, I. W. Choi, S. J. Choi, Y. Jo, H.-B. Kim, S.-I. Mo, Y.-K. Kim, H. Lee, N. G. An, S. Cho, W. R. Tress, S. M. Zakeeruddin, A. Hagfeldt, J. Y. Kim, M. Grätzel and D. S. Kim, *Science*, 2022, **375**, 302–306.
3 J. Y. Kim, J.-W. Lee, H. S. Jung, H. Shin and N.-G. Park, *Chem. Rev.*, 2020, **120**, 7867–7918.
4 Q. Dong, Y. Fang, Y. Shao, P. Mulligan, J. Qiu, L. Cao and J. Huang, *Science*, 2015, **347**, 967–970.
5 S. D. Stranks, G. E. Eperon, G. Grancini, C. Menelaou, M. J. P. Alcocer, T. Leijtens, L. M. Herz, A. Petrozza and H. J. Snaith, *Science*, 2013, **342**, 341–344.
6 B. Li, B. Chang, L. Pan, Z. Li, L. Fu, Z. He and L. Yin, *ACS Energy Lett.*, 2020, **5**, 3752–3772.
7 J. Chen and N.-G. Park, *ACS Energy Lett.*, 2020, **5**, 2742–2786.
8 W. A. Dunlap-Shohl, Y. Zhou, N. P. Padture and D. B. Mitzi, *Chem. Rev.*, 2019, **119**, 3193–3295.
9 F. Zhang and K. Zhu, *Adv. Energy Mater.*, 2020, **10**, 1902579.
10 J. Chen and N.-G. Park, *Adv. Mater.*, 2019, **31**, 1803019.
11 T. Li, Y. Pan, Z. Wang, Y. Xia, Y. Chen and W. Huang, *J. Mater. Chem. A*, 2017, **5**, 12602–12652.
12 G. Yang, C. Chen, F. Yao, Z. Chen, Q. Zhang, X. Zheng, J. Ma, H. Lei, P. Qin, L. Xiong, W. Ke, G. Li, Y. Yan and G. Fang, *Adv. Mater.*, 2018, **30**, 1706023.
13 L. Qiu, Z. Liu, L. K. Ono, Y. Jiang, D.-Y. Son, Z. Hawash, S. He and Y. Qi, *Adv. Funct. Mater.*, 2019, **29**, 1806779.
14 W. Ke, G. Fang, Q. Liu, L. Xiong, P. Qin, H. Tao, J. Wang, H. Lei, B. Li, J. Wan, G. Yang and Y. Yan, *J. Am. Chem. Soc.*, 2015, **137**, 6730–6733.
15 P. Tiwana, P. Docampo, M. B. Johnston, H. J. Snaith and L. M. Herz, *ACS Nano*, 2011, **5**, 5158–5166.
16 D. Wang, T. He, S. Li, Y. Jiang and M. Yuan, *ACS Appl. Energy Mater.*, 2022, **5**, 5340–5347.
17 W. Long, A. He, S. Xie, X. Yang and L. Wu, *Energies*, 2022, **15**, 3211.
18 C. Wang, L. Guan, D. Zhao, Y. Yu, C. R. Grice, Z. Song, R. A. Awni, J. Chen, J. Wang, X. Zhao and Y. Yan, *ACS Energy Lett.*, 2017, **2**, 2118–2124.
19 L. Kavan, L. Steier and M. Grätzel, *J. Phys. Chem. C*, 2017, **121**, 342–350.
20 S. Jeong, S. Seo, H. Park and H. Shin, *Chem. Commun.*, 2019, **55**, 2433–2436.
21 S. Seo, S. Shin, E. Kim, S. Jeong, N.-G. Park and H. Shin, *ACS Energy Lett.*, 2021, **6**, 3332–3341.
22 S. Seo, S. Jeong, H. Park, H. Shin and N.-G. Park, *Chem. Commun.*, 2019, **55**, 2403–2416.
23 C. Bae, H. Kim, E. Kim, H. G. Park and H. Shin, *Chem. Mater.*, 2018, **30**, 4748–4754.
24 S. Seo, S. Jeong, C. Bae, N.-G. Park and H. Shin, *Adv. Mater.*, 2018, **30**, 1801010.
25 J. W. Elam, D. A. Baker, A. J. Hryn, A. B. F. Martinson, M. J. Pellin and J. T. Hupp, *J. Vac. Sci. Technol., A*, 2008, **26**, 244–252.
26 M. N. Mullings, C. Hägglund and S. F. Bent, *J. Vac. Sci. Technol., A*, 2013, **31**, 061503.
27 Z. Ye, Q. Wei, Y. Cheng, X. Zhang, P. Ji, X. Ren, L. Zan and F. Fu, *Ceram. Int.*, 2022, **48**, 28092–28101.
28 J. Xie, K. Huang, X. Yu, Z. Yang, K. Xiao, Y. Qiang, X. Zhu, L. Xu, P. Wang, C. Cui and D. Yang, *ACS Nano*, 2017, **11**, 9176–9182.
29 H. Wang, H. Liu, F. Ye, Z. Chen, J. Ma, J. Liang, X. Zheng, C. Tao and G. Fang, *J. Power Sources*, 2021, **481**, 229160.
30 J. Hofmann, G. Just, W. Pritzkow and H. Schmidt, *J. Prakt. Chem.*, 1992, **334**, 293–297.
31 J. Wang, H. Li, S. Meng, X. Ye, X. Fu and S. Chen, *RSC Adv.*, 2017, **7**, 27024–27032.
32 K. Gawlak, D. Popiołek, M. Pisarek, G. D. Sulka and L. Zaraska, *Materials*, 2022, **15**, 3848.
33 T. Jia, W. Wang, F. Long, Z. Fu, H. Wang and Q. Zhang, *J. Phys. Chem. C*, 2009, **113**, 9071–9077.
34 A. R. Babar, S. S. Shinde, A. V. Moholkar, C. H. Bhosale, J. H. Kim and K. Y. Rajpure, *J. Alloys Compd.*, 2010, **505**, 416–422.
35 X. S. Peng, G. W. Meng, X. F. Wang, Y. W. Wang, J. Zhang, X. Liu and L. D. Zhang, *Chem. Mater.*, 2002, **14**, 4490–4493.
36 P. Baraneedharan, S. Imran Hussain, V. P. Dinesh, C. Siva, P. Biji and M. Sivakumar, *Appl. Surf. Sci.*, 2015, **357**, 1511–1521.
37 J. Chen, X. Zhao, S.-G. Kim and N.-G. Park, *Adv. Mater.*, 2019, **31**, 1902902.
38 H. B. Lee, N. Kumar, M. Ovhal, Y. Song and J.-W. Kang, *Adv. Funct. Mater.*, 2020, **30**, 2001559.
39 C. Wang, J. Wu, X. Liu, S. Wang, Z. Yan, L. Chen, G. Li, X. Zhang, W. Sun and Z. Lan, *J. Alloys Compd.*, 2021, **886**, 161352.

40 W. Ahmad, D. Liu, W. Ahmad, Y. Wang, P. Zhang, T. Zhang, H. Zheng, Z. D. Chen and S. Li, *IEEE J. Photovolt.*, 2019, **9**, 200–206.
41 C. Ma and N.-G. Park, *ACS Energy Lett.*, 2020, **5**, 3268–3275.
42 K. Deng, Q. Chen and L. Li, *Adv. Funct. Mater.*, 2020, **30**, 2004209.
43 D. Yang, R. Yang, K. Wang, C. Wu, X. Zhu, J. Feng, X. Ren, G. Fang, S. Priya and S. Liu, *Nat. Commun.*, 2018, **9**, 3239.
44 A.-N. Cho, N. Chakravarthi, K. Kranthiraja, S. S. Reddy, H.-S. Kim, S.-H. Jin and N.-G. Park, *J. Mater. Chem. A*, 2017, **5**, 7603–7611.
45 J.-H. Kim, S.-G. Kim and N.-G. Park, *ACS Energy Lett.*, 2021, **6**, 3435–3442.
46 D.-H. Kang, C. Ma and N.-G. Park, *ACS Appl. Mater. Interfaces*, 2022, **14**, 8984–8991.
47 M. Kim, I.-W. Choi, S. J. Choi, J. W. Song, S.-I. Mo, J.-H. An, Y. Jo, S. Ahn, S. K. Ahn, G.-H. Kim and D. S. Kim, *Joule*, 2021, **5**, 659–672.
48 W. Fan, Y. Shen, K. Deng, Q. Chen, Y. Bai and L. Li, *Nano Energy*, 2022, **100**, 107518.
49 J. H. Heo, M. S. You, M. H. Chang, W. Yin, T. K. Ahn, S.-J. Lee, S.-J. Sung, D. H. Kim and S. H. Im, *Nano Energy*, 2015, **15**, 530–539.
50 Y. Qiang, Y. Xie, Y. Qi, P. Wei, H. Shi, C. Geng and H. Liu, *Sol. Energy*, 2020, **201**, 523–529.
51 M.-J. Choi, Y.-S. Lee, I. H. Cho, S. S. Kim, D.-H. Kim, S.-N. Kwon and S.-I. Na, *Nano Energy*, 2020, **71**, 104639.
52 S.-N. Kwon, J.-H. Yu and S.-I. Na, *J. Alloys Compd.*, 2019, **801**, 277–284.
53 L. Meng, C. Sun, R. Wang, W. Huang, Z. Zhao, P. Sun, T. Huang, J. Xue, J.-W. Lee, C. Zhu, Y. Huang, Y. Li and Y. Yang, *J. Am. Chem. Soc.*, 2018, **140**, 17255–17262.
54 Z. Li, R. Wang, J. Xue, X. Xing, C. Yu, T. Huang, J. Chu, K.-L. Wang, C. Dong, Z. Wei, Y. Zhao, Z.-K. Wang and Y. Yang, *J. Am. Chem. Soc.*, 2019, **141**, 17610–17616.
55 T. Bu, J. Li, F. Zheng, W. Chen, X. Wen, Z. Ku, Y. Peng, J. Zhong, Y.-B. Cheng and F. Huang, *Nat. Commun.*, 2018, **9**, 4609.
56 C.-C. Chung, S. Narra, E. Jokar, H.-P. Wu and E. W.-G. Diau, *J. Mater. Chem. A*, 2017, **5**, 13957–13965.
57 R. S. Sanchez, V. Gonzalez-Pedro, J.-W. Lee, N.-G. Park, Y. S. Kang, I. Mora-Sero and J. Bisquert, *J. Phys. Chem. Lett.*, 2014, **5**, 2357–2363.
58 L. Zheng, Y. Ma, L. Xiao, F. Zhang, Y. Wang and H. Yang, *ACS Appl. Mater. Interfaces*, 2017, **9**, 14129–14135.
59 J. Chen, S.-G. Kim and N.-G. Park, *Adv. Mater.*, 2018, **30**, 1801948.
60 J. H. Lee, D. Shin, R. Rhee, S. Yun, K. M. Yeom, D. H. Chun, S. Lee, D. Kim, Y. Yi, J. H. Noh and J. H. Park, *J. Phys. Chem. Lett.*, 2019, **10**, 6545–6550.
61 N. Ahn, K. Kwak, M. S. Jang, H. Yoon, B. Y. Lee, J.-K. Lee, P. V. Pikhitsa, J. Byun and M. Choi, *Nat. Commun.*, 2016, **7**, 13422.